RSC Pharmaceutics

ROYAL SOCIETY OF CHEMISTRY

PAPER

View Article Online
View Journal | View Issue

Cite this: *RSC Pharm.*, 2026, **3**, 220

Spray-dried inhalable nano-embedded microparticles of isoniazid and pyridoxine hydrochloride for pulmonary tuberculosis

Eknath Kole, [a,d] Krishna Jadhav, [b] Priya Chichmalkar,[a] Rahul K. Verma, [b] Arun Mujumdar[c] and Jitendra Naik *[a]

Tuberculosis (TB) is the second deadliest communicable disease caused by *Mycobacterium tuberculosis* and mainly affects the lungs. Current TB therapy typically involves the oral administration of antitubercular drugs (ATDs). However, this approach is often associated with challenges, such as drug toxicity, suboptimal pulmonary drug concentration, and issues with patient adherence. Moreover, isoniazid (INH) therapy frequently induces pyridoxine (PDX) deficiency in TB patients, potentially leading to neuropathy. In this study, INH–PDX nano-embedded microparticles (NEMs) were developed as a dry powder formulation to enhance pulmonary TB treatment. The formulation was optimised using a microreactor through a three-factor, three-level Box–Behnken design (BBD). The optimised dry powder achieved a product yield of 48.36% (w/w) and a drug-loading efficiency of 24.14 ± 2.86% (w/w). The particles exhibited a spherical morphology. Furthermore, aerosolization performance demonstrated the formulation's suitability for deep lung deposition, with a mass median aerodynamic diameter (MMAD) of 5.97 ± 1.10 μm, a fine particle fraction (FPF) of 36.63 ± 3.12%, and a geometric standard deviation (GSD) of 1.73 ± 0.23. In conclusion, the Design of Experiments (DoE)-based optimisation approach successfully optimised the process parameters and produced a dry powder formulation suitable for pulmonary delivery in patients with TB, addressing both treatment efficacy and neuropathy concerns.

Received 24th April 2025,
Accepted 31st October 2025

DOI: 10.1039/d5pm00118h

rsc.li/RSCPharma

1. Introduction

Tuberculosis (TB) is the second deadliest communicable disease caused by *Mycobacterium tuberculosis* (Mtb), which mainly affects the lungs. According to the latest World Tuberculosis Report 2024, in 2023, there were 10.8 million new cases and 1.25 million deaths due to TB.[1,2] To effectively combat TB, treatment strategies must address two key challenges: eliminating dormant Mtb within granulomas and eradicating actively replicating mycobacteria in cavitary lesions. This dual approach required tailored therapeutics capable of targeting both persistent and active TB infections.[3] Typical treatment of TB comprises a multidrug therapy that includes first-line antitubercular drugs (ATDs) like isoniazid (INH), rifampicin, rifabutin, pyrazinamide, and ethambutol, administered daily for eight weeks, followed by a further 16 weeks of INH and rifampicin administration.[4] However, this prolonged treatment duration (16–24 weeks) and high pill burden often lead to challenges, including reduced patient compliance due to side effects and drug interactions, ultimately increasing the risk of treatment failure and the rise of drug-resistant TB (DR-TB).[5]

INH is a key drug in TB treatment because of its potent bactericidal activity against Mtb and utility in preventive treatment. It is rapidly absorbed, achieving peak concentration within 1–2 hours of administration, but is associated with adverse effects such as peripheral neuropathy and neurotoxicity.[6] To mitigate these neurotoxic effects, pyridoxine hydrochloride (PDX) (vitamin B6) is co-administered with INH, especially in individuals at a higher risk of neuropathy. This approach is effective in preventing INH-induced neuropathy but increases the pill burden and may present pharmacokinetic challenges, such as the risk of under- or over-supplementation with PDX.[7–9] The complexity of TB treatment, including the need for multiple drugs, high cost, and adverse side effects, contributes to poor adherence. This problem is further compounded by the palatability of ATD formulations, particularly in paediatric patients, leading to missed doses and an increased risk of treatment failure.[10] More than 10% of TB

[a]*Department of Pharmaceutical Technology, University Institute of Chemical Technology, KBC North Maharashtra University, Jalgaon, MS 425001, India. E-mail: jbnaik@nmu.ac.in, jitunaik@gmail.com*
[b]*Pharmaceutical Nanotechnology Lab, Institute of Nano Science and Technology, Sahibzada Ajit Singh Nagar, Mohali, Punjab 140306, India*
[c]*Department of Bioresource Engineering, Macdonald College, McGill University, Quebec, Canada*
[d]*University Department of Pharmaceutical Sciences, MGM University, Chhatrapati Sambhajinagar, M.S. 431001, India*

patients on standard therapy with first-line drugs, including INH, discontinue treatment due to drug-induced side effects such as neuropathy and hepatotoxicity.[11] Developments in pharmaceutical technology have enabled the fabrication of novel drug delivery systems such as nanoparticles, liposomes, and microparticles, allowing for the simultaneous, sustained release of multiple drugs. These systems not only enhance bioavailability and enable targeted delivery but also offer stability for INH, which is susceptible to degradation, and precise dosing of PDX.[12]

Co-delivery of several drugs commonly used in TB therapy is implemented to reduce the risk of drug resistance, reduce the duration of therapy, and lower the chance of setback.[13] Various drug delivery systems are employed to augment the therapeutic effectiveness of antibiotics. These approaches include polymeric nanoparticles, microparticles, dry powder inhalation, dendrimers, liposomes, nanostructured lipid nanoparticles, *etc*.[14] Additionally, nanocarriers have been extensively utilized to provide high drug loading capacities, enable sustained or controlled release of drugs, and ensure targeted delivery, while maintaining safety and biocompatibility for human applications.[15] Biodegradable polymers such as chitosan oligosaccharide (COS) and dextran sulphate (DS) have been widely explored for drug delivery applications because of their biocompatibility and controlled release properties.[16] Previous studies demonstrated their efficacy in delivering antitubercular drugs, including isoniazid (INH)[17] and rifampicin, highlighting their potential for targeted and sustained therapeutic delivery.[18]

The use of inhalable dry powder of antibiotics for local drug delivery is gaining attention because it enhances targeted delivery to the lungs, reduces DR, and minimises systemic drug exposure. This approach is particularly valuable because the lungs are the main site of Mtb infections.[19] The effectiveness of the inhaled dose relies on the characteristics of the dry powder and its compatibility with the inhalation device.[20] A consistent and predictable delivered dose is crucial, and research highlights the complex interaction between powder properties and device characteristics that affect aerosolization performance.[21] Quality-by-Design (QbD) guided optimization of the formulation will enhance the practicality and therapeutic efficacy of nano-embedded microparticles (NEMs). By combining microreactor synthesis with the spray drying technique, this approach ensures the development of an efficient inhalable dry powder formulation with well-defined critical quality attributes. Design of experiments (DoE) was used to optimise nanoparticles (NPs) for spray drying and to formulate the dry powder *via* a QbD-based approach.[22–27] This study considers a new perspective by exploring QbD strategies for the development of dry powder formulations using COS and DS as polyelectrolyte complex NPs using microreactor techniques, followed by spray drying. We formulated the co-delivery of INH and PDX drugs by co-loading them into a polyelectrolyte complex of polymeric nanoparticles and administered them as an INH–PDX–NEM inhalable dry powder. The reason behind this strategy is to employ combination therapy, which helps prevent the emergence of drug resistance while utilizing inhalation as a method of drug delivery. This approach ensures that the drug is directly deposited at the target site. This method also aims to improve patient compliance by reducing systemic exposure and related toxicities. To achieve these goals, we employed the Box–Behnken design (BBD) as a DoE approach for optimizing the development of NPs using a microreactor, focusing on refining the process parameters. The optimized NPs were spray dried to obtain microparticles as a dry powder, which was subjected to comprehensive solid-state characterization, drug content analysis, surface morphology evaluation, *in vitro* aerosolization behaviour and drug release studies, stability assessment of the nanosuspension and dry powder and *in vitro* antibacterial testing to confirm their effectiveness in TB patients.[5]

In particular, codelivery systems that combine INH and PDX have the potential not only to streamline, aiming to improve both the safety and efficacy of TB treatment, but also to ensure that an appropriate balance of PDX is delivered in conjunction with INH, thus preventing neuropathy more effectively.

2. Methods

2.1. Materials

Isoniazid (INH, purity ≥99.5%) was gifted by Lupin Ltd, Chhatrapati Sambhajinagar, and pyridoxine hydrochloride (PDX, purity ≥98%), low molecular weight chitosan oligosaccharide (COS) (~3000.00) dextran sulfate (DS), polyvinylpyrrolidone (K-30), and paraformaldehyde were purchased from Sisco Research Laboratories Pvt. Ltd, Mumbai, India. Triton X-100, 4′,6-diamidino-2-phenylindole dihydrochloride (DAPI), fluorescein Isothiocyanate (FITC) and trypsin were procured from Sigma-Aldrich (St Louis, MO, USA). Acetonitrile and methanol were procured from Merck (Mumbai, India). Sodium hydroxide, hydrochloric acid, glacial acetic acid, phosphate-buffered saline (PBS), ethylenediaminetetraacetic acid (EDTA), and Dulbecco's modified Eagle's medium (DMEM) were procured from Hi-media, Mumbai, India and ThermoFisher Scientific, Mumbai, India. RAW 264.7 and MTCC 300 (H37Ra, BSL-2), and *M. tuberculosis* bacteria, were supplied by the National Centre for Cell Science, Pune. All other chemicals and reagents used were of analytical grade.

2.2. Preparation of nanoparticles

Isoniazid (INH) and pyridoxine hydrochloride (PDX)-loaded polyelectrolyte complex of chitosan oligosaccharide-dextran sulphate nanoparticles (INH–PDX COSDSNPs) were fabricated using a microreactor (AmAR 2 metal), following the methodology previously reported by Kole *et al.*[28] Briefly, 50 mg of COS was dissolved in 0.5% acetic acid solution and magnetically stirred (LABQUEST, BOROSIL) for 30 min to obtain a clear solution, which was referred to as solution A (50 mL), and INH (10 mg) and PDX (5 mg) were dissolved in 2 mL of distilled water and then added dropwise to solution A using a syringe,

and 0.1% w/w PVP K-30 was introduced as a stabiliser in solution A. Moreover, an aqueous solution of 0.1% w/v DS was prepared and referred to as solution B (50 mL). Both solutions were stirred constantly for 30 min at 600 rpm. Both solutions were subjected to ultrasonication for 3–5 min and then filtered using a PVD filter (0.45 μm filter, Ecostat). Solutions A and B were then passed through a syringe (connected to a microreactor) *via* an infuser (Uni Labs) to maintain a constant flow rate (24 mL h^{-1}). The nanosuspension was collected through a microreactor outlet under continuous stirring at 600 rpm at room temperature (25 ± 2 °C). Drug-loaded NPs from the nanosuspension were washed twice and collected by centrifugation at 15 000 rpm for 30 min at 4 °C. Blank COSDSNPs were fabricated using a similar approach and deprived of drugs.

2.3. Nanoparticle characterisation

Physiochemical characterisation of both blank nanoparticles and INH–PDX–COSDSNPs was performed using dynamic light scattering (Nano ZS 90 Zetasizer, Malvern Instruments Ltd, UK). Samples were prepared by diluting 100 μL of the nanosuspension in 2 mL of double-distilled water (1 : 20 dilution) and were analysed in disposable cuvettes at 25 °C. The measurements were conducted at a fixed scattering angle of 173° with an acquisition time of 120 s per run. Independent measurements were performed to determine the average particle size and polydispersity index (PDI).

The surface charge (zeta potential) of INH–PDX–COSDSNPs was measured using electrophoretic light scattering on a Zetasizer (Nano ZS 90, Malvern Instruments Ltd, UK). Samples were diluted in water, allowed to equilibrate at 25 °C, and analysed using a Surface Zeta Potential Cell (Malvern), which is designed for accurate electrophoretic mobility measurements.[29] The experiment was conducted thrice, and the results are presented as mean ± SD.

2.4. Encapsulation efficiency and drug loading

The drug encapsulation efficiency of INH–PDX COSDSNPs was quantified using UV-Vis spectroscopy. The nanosuspension was centrifuged (10 000 rpm, 4 °C; Thermo Scientific Sorvall ST 8R) to separate the free drug from the polyelectrolyte complex. The supernatant containing unentrapped drug was analysed using a UV-2600i spectrophotometer (Shimadzu, Japan) by measuring INH at 262 nm and PDX at 246 nm. Entrapment efficiency (EE) and drug loading (DL) were calculated using a pre-established calibration curve (R^2 = 0.9986) and standard equations. All measurements were performed in triplicate (n = 3).[28]

$$\text{Drug loading}\left(\%\frac{\text{w}}{\text{w}}\right) = \frac{\text{Weight of entrapped drug}}{\text{Weight of nanoparticles}} \times 100 \quad (1)$$

$$\text{Entrapment efficiency}\,(\%) = \frac{\text{Total drug added} - \text{unbound drug}}{\text{Total drug added}} \times 100. \quad (2)$$

2.5. Particle morphology

The surface morphology of the optimised INH–PDX–COSDSNPs was investigated using field-emission scanning electron microscopy (FE-SEM) (JSM IT300LV, JEOL, Japan). The sample was affixed to aluminium stubs mounted on a holder and coated with gold using a coater (JCE-3000FC, JEOL, Japan) for 50 s. Subsequently, photomicrographs were captured using a secondary electron detector at an accelerating voltage of 10 kV.[28]

2.6. Experimental design

The BBD of three factors at three levels was used to optimize the nanoformulation variables for fabricating INH and PDX-loaded COSDSNPs to estimate the main effects. We performed initial experiments to determine the primary factors and their appropriate ranges for optimizing the nanoformulation. The experimental design for the optimization of nanoformulations using BBD was used to create the models using Design Expert® V.13 (Stat-Ease Inc., Minneapolis, MN). The BBD assesses the experimental error and the precision of the design when optimizing nanosuspensions. The effects of process parameters (independent variables) were scientifically observed, such as the amount of polymers (X_1 and X_2), percentage of stabiliser (X_3), drug concentration on average particle size (Y_1), polydispersity index (Y_2), and zeta potential (Y_3). Furthermore, we selected Y_1 as the average particle size, Y_2 as the PDI, and Y_3 as the zeta potential, which served as the dependent variable or response. We examined three levels for the independent variables: low (−1), medium (0), and high (+1), as outlined in Table 1. The BBD is suitable for determining the impact of independent variables, that is, polymers, stabilisers, and drug concentration, on their allied outcomes on the dependent variable. The concentration and percentage of polymers and stabilisers were specified as independent variables. The developed NH–PDX-loaded COSDSNP formulations were characterised with respect to crucial variables including particle size, PDI, and zeta potential. In accordance with the proposed BBD, 17 experimental runs (including three centre

Table 1 Independent variables (range) and dependent variables (constraint of variables) and their levels for the Box–Behnken design

		Levels		
Input variables (independent variables)		Low (−1)	Medium (0)	High (+1)
Numeric factors	X_1: amount of chitosan (mg mL^{-1}, w/v)	−1	0	1
	X_2: amount of dextran sulphate (%, w/v)	−1	0	1
	X_3: amount of PVP K-30 (%, w/v) (stabilizer)	−1	0	1

Responses (dependent variables)	Constraints
Y_1: particle size (nm)	Minimum
Y_2: polydispersity index (PDI)	Minimum
Y_3: zeta potential (mV)	±less than 30

points) were performed in triplicate and characterised, as detailed in Table 2. Polynomial equations representing the main effects, interaction effects, and linear and two-factor interaction (2FI) effects of the independent formulation variables demonstrated significant impacts on the measured responses. The validity of the model was evaluated based on two main criteria: (1) the predicted coefficient of determination (Pred R^2) would be in close contact with the adjusted coefficient of determination (Adj R^2), and (2) the probability value from the one-way analysis of variance (ANOVA) should be greater than the *F*-value. Additionally, three-dimensional response surface and contour plots were used to visually illustrate the effects of the independent variables on the dependent responses. These graphical tools facilitated the identification of optimal experimental conditions by illustrating the relationships between input variables and the resulting responses.[30]

2.7. Preparation and characterisation of dry powder

INH and PDX-loaded-COSDSNP powders or microparticles from nanosuspensions (resuspended nanoparticles) were prepared using a laboratory spray dryer (Spray Mate JISL, Mumbai) with a 0.5 mm nozzle atomiser. The feedstock solution (nanosuspension) was prepared using a microreactor (the procedure is described in section 2.2). The formulations were dried under the following operating conditions: inlet temperature (110 °C); outlet temperature (50–60 °C); atomisation pressure (1.2 kg cm^{-2}), feed flow rate (6 mL min^{-1}); and vacuum range (100–110 mm). To prepare inhalable microparticles, INH–PDX-loaded COSDSNPs were spray-dried with mannitol.[31] Before proceeding with spray drying, the nanosuspension was ultracentrifuged (10 000 rpm for 30 min) to prepare pellets of nanoparticles or sedimentation of nanoparticles to be resuspended in Milli-Q water containing mannitol to obtain a nanoparticle to excipient ratio of 1 : 2 (w/w). The amount of mannitol was 5% w/w of the total concentration of excipients. The nanosuspension was pumped into the feeding system of a spray dryer. The resulting spray-dried powders were collected from the cyclone separator in a collector vessel, stored in a sealed glass bottle, and stored in a desiccator containing silica gel at room temperature until further analysis. As noticeable indicators of the effectiveness of the spray-drying approach, critical parameters, including the process yield, particle size, and surface morphology, were studied across various process environments.

2.7.1. Product yield. The spray-dried powder yield was determined based on the weight of dry powder obtained from the collection vessel and cyclone separator and compared to the total solid weight of drugs with polymers of the feedstock solution. The yield of the spray-dried powder was calculated using the given formula.[32]

$$\text{Product yield} = \frac{\text{Weight of spray dried microparticles}}{\text{Total weight of all ingredients of formulation}} \times 100. \quad (3)$$

2.7.2. Particle morphology. The surface morphology of the dry powder of the INH–PDX–NEM spray-dried particles was imaged using FE-SEM (JSM IT300LV, JEOL, Japan). The spray-dried particles were imaged using the method described (section 2.5).[33]

2.7.3. Redispersibility. To confirm the resuspendability of the formulated INH–PDX-loaded nano-embedded microparticle (INH–PDX–NEM) spray-dried powder, 2 mg of the powder was redispersed in 2 mL of double-distilled water. The particle size and zeta potential of the redispersed nanoparticles were then assessed with the previously described method (section 2.3).[28]

Table 2 Box–Behnken design independent variables and conforming results for the dependent variables

	Independent variables			Dependent variables		
Run	Factor 1 (X_1) *A*: chitosan (mg)	Factor 2 (X_2) *B*: dextran sulfate (%)	Factor 3 (X_3) *C*: PVP K-30 (%)	Response 1 (Y_1) Particle size (nm)	Response 2 (Y_2) PDI	Response 3 (Y_3) Zeta potential (mV)
1	0	−1	−1	215.26 ± 8.39	0.212 ± 0.02	−15.2 ± 0.51
2	1	−1	0	277.5 ± 7.74	0.131 ± 0.03	−9.8 ± 0.023
3	1	0	1	282.5 ± 1.82	0.135 ± 0.01	−17.07 ± 2.14
4	−1	−1	0	225.6 ± 6.60	0.161 ± 0.002	−24 ± 0.31
5	0	0	0	232.56 ± 1.78	0.214 ± 0.003	−16.7 ± 0.26
6	−1	0	−1	189.06 ± 5.00	0.27 ± 0.001	−14.8 ± 3.23
7	0	1	1	287.5 ± 4.10	0.12 ± 0.0008	−16.23 ± 0.42
8	0	0	0	225.2 ± 6.95	0.214 ± 0.007	−17.66 ± 0.45
9	0	0	0	204.74 ± 6.15	0.21 ± 0.001	−18.6 ± 0.26
10	0	0	0	221.34 ± 3.79	0.224 ± 0.009	−19.33 ± 0.32
11	0	−1	1	219 ± 2.61	0.149 ± 0.008	−8.9 ± 0.398
12	−1	1	0	175.9 ± 1.74	0.207 ± 0.005	−17.9 ± 0.55
13	1	1	0	269.9 ± 2.01	0.412 ± 0.02	−17.39 ± 0.27
14	1	0	−1	209.08 ± 1.04	0.221 ± 0.02	−19.83 ± 2.01
15	0	1	−1	188.18 ± 5.62	0.226 ± 0.01	−22.25 ± 3.58
16	−1	0	1	464.16 ± 9.26	0.212 ± 0.02	−19.83 ± 2.01
17	0	0	0	204.74 ± 6.53	0.28 ± 0.002	−18.6 ± 0.26

2.8. Solid state characterisation (additional powder characterisation)

2.8.1. Fourier transform infrared spectroscopy (FT-IR). FT-IR spectra were recorded to assess the interactions between the polymers and drugs using a Spectrum Two spectrometer (PerkinElmer, MA, USA) equipped with a universal attenuated total reflectance (ATR) accessory (UATR, single Reflection Diamond/ZnSe). A small quantity of each sample was placed in the ATR cell for spectral analysis. The spectra were acquired in the transmission mode at a resolution of 4 cm^{-1} under a dry air purge, with 16 scans accumulated in the ATR mode.[34] The IR spectra for CS, DS, INH, PDX, and INH–PDX–NEM powders were obtained across the range from 4000 to 400 cm^{-1}.

2.8.2. Differential scanning calorimetry (DSC). The thermal properties of the CS, DS, INH, PDX, INH, and PDX–NEM powders were evaluated using a differential scanning calorimeter (DSC-7020, Hitachi High-Tech Corporation, Japan). Each sample (5 mg) was placed in aluminium crucibles, hermetically sealed, and heated from 30 to 700 °C at a rate of 20 °C min^{-1}; the nitrogen gas flow was maintained. The resulting thermograms were processed using TA7000 software (Hitachi High-Tech Corporation, Japan).[35]

2.8.3. Thermogravimetric analysis (TGA). The thermal stability of CS, DS, INH, and PDX and the dried powders of INH–PDX–NEM were determined using a TGA-55 thermogravimetric analyser (TA Instruments, UK). Briefly, 5 mg of each sample was loaded into a platinum pan at a heating rate of 20 °C min^{-1} over a temperature range of 20–600 °C under a nitrogen atmosphere, purging gas at 50 mL min^{-1}. Data analysis was conducted using TA Instrument Universal Analysis 2000 4.5 A software, and weight loss (%) graphs were plotted as a function of temperature.[36]

2.8.4. X-ray diffraction (XRD). The physical characteristics, specifically the crystallinity, of the powders were analysed using a Bruker AXS D8 Focus XRD diffractometer equipped with a Copper X-ray source (Cu Kα; λ = 1.54 Å). The instrument was operated at a voltage of 40 kV and a current of 40 mA. Powder samples of CS, DS, INH, PDX, and INH–PDX–NEM were loaded into plastic sample holders, and the surfaces were levelled using a glass slide.[37] The XRD patterns of the samples were recorded at room temperature within an angular scanning range of 5–60° (2θ) with a step size of 0.2° and a scan rate of 1° min^{-1}.

2.9. *In vitro* aerosolization performance

The *in vitro* aerodynamic performance of the INH–PDX–NEM dry powder formulation was evaluated using a Next-Generation Impactor (NGI, Copley Scientific, UK) in conjunction with a Rotahaler® device (Cipla, Mumbai, India). Approximately 25 mg of the INH–PDX–NEM powder was precisely weighed and filled into hard gelatin capsules (size-3). These capsules were later inserted into the sample holder of Rotahaler®, which was securely attached to the induction port of the NGI system. The NGI apparatus was operated at an airflow rate of 60 L min^{-1} for 10 s, driven by a high-capacity pump (HCP5, Copley, UK), and monitored using a digital flow meter (DFM2, Copley Scientific, UK). Upon actuation, the Rotahaler® punctured the capsule, releasing the INH–PDX–NEM dry powder into the airflow at a controlled rate of 60 L min^{-1}.

The NGI classified the aerosolised particles based on their aerodynamic diameter, with each stage corresponding to an effective cut-off diameter of 8.06, 4.46, 2.82, 1.66, 0.94, 0.55, and 0.34 μm, representing different deposition sites within the respiratory tract.[38] During APSD testing with the Andersen Cascade Impactor, a preseparator was used to capture large carrier particles and agglomerates, helping to avoid overloading of the impactor stages and to obtain an accurate measurement of the respirable fraction, in line with pharmacopeial recommendations. The mass of the powder deposited at each NGI stage was quantified gravimetrically, with all experiments conducted in triplicate to ensure reproducibility. Key aerodynamic parameters, including the emitted dose (ED), mass median aerodynamic diameter (MMAD), geometric standard deviation (GSD), and fine particle fraction (FPF), were subsequently calculated to assess the performance of the dry powder formulation.

2.10. *In vitro* drug release

In the study, the *in vitro* release of INH, PDX, and INH–PDX–NEM was evaluated using a release medium of 900 mL phosphate buffered saline (PBS, pH 7.4) at a temperature of 37.5 °C ± 0.5 °C and stirred at 50 rpm. Pure INH, PDX, and INH–PDX–NEM were placed in dialysis bags (molecular weight = 12–14 kDa, Sigma Aldrich, USA) with 2 mL of each sample. The bags were then submerged in a glass vessel containing a release medium. Each bag contained 50 mg of the drug and a dry powder formulation. At the stated times (15, 30, 45, 60, and 90 min, and 2, 4, 6, 8, 12, 16, 24, 48, and 72 h), 5 mL aliquots were taken and replaced with an equal volume of fresh medium to maintain sink conditions. Aliquots were passed through 0.2 μm PVDF syringe filters to remove any residual substances, and the resulting supernatants were analysed for drug content. According to the established methods, the amounts of INH and PDX released from the INH–PDX–NEM formulation were assessed using a UV-Vis spectrophotometer. Sink conditions were consistently maintained throughout the experiment, with sampling conducted in triplicate (n = 3).[39]

2.11. Stability study

Stability studies were conducted on the optimised nanosuspension (INH–PDX–CSDSNPs) and dry powder formulation (INH–PDX–NEM) over a period of six months at 25 ± 2 °C. The INH–PDX–CSDSNPs and dry powder formulations of INH–PDX–NEM were stored in amber glass vials with tightly sealed lids at 25 °C and 60% relative humidity (RH) for six months, in accordance with ICH guidelines for long-term stability assessment.[40] Evaluations were evaluated at definite time points (0, 1, 2, 3, 4, 5, and 6 months) to determine the particle size, PDI, and zeta potential.

2.12. Anti-mycobacterial activity

The well-diffusion method was employed to evaluate the antimicrobial activity of pure INH and INH–PDX–NEM. An

aqueous solution of INH at the same concentration as the formulations, along with blank nanoparticles, served as controls. The *Mycobacterium tuberculosis* strain MTCC 300 (H37Ra, BSL-2) was used to assess antibacterial efficacy. A bacterial suspension was prepared according to the 0.5 McFarland standard. Subsequently, 500 μL of the diluted log-phase culture was transferred to microcentrifuge tubes. To each tube, 10 μL of nano-embedded microparticles or aqueous solutions of pure INH at various concentrations were added, followed by incubation at 37 °C for 15 days. After incubation, the contents of each tube were transferred to 96-well plates, and 250 μg mL^{-1} of MTT solution was added to each well. Blank nanoparticles (100 μL) were added to three wells as the negative control, while INH served as the positive control. The plates were incubated at 37 °C for an additional 24 h, after which absorbance was measured at 490 nm and 595 nm using an ELISA plate reader (iMark, Bio-Rad). The minimum inhibitory concentration (MIC) of pure INH and INH–PDX–NEM was determined as the lowest concentration that completely inhibited bacterial growth around the wells.[41]

2.13. Cellular uptake study

Nanoparticle localisation and intracellular distribution were studied by fluorescence microscopy using a cellular uptake assay. RAW 264.7 cell lines were harvested *via* trypsinisation with an EDTA–trypsin solution (0.25%) from T-75 cell culture flasks, and cell counts were performed using a haemocytometer (HBG, Germany). Cells were seeded onto poly-L-lysine-coated coverslips in 6-well microplates at a density of 2×10^4 cells per well and incubated in DMEM at 37 °C in a humidified CO_2 incubator (5% CO_2, HEPA class 100, Thermo Fisher Scientific, USA) for 24 h to ensure adhesion. The medium was then removed, and cells were treated with COSDSNPs (1 mg mL^{-1} in DMEM). After the specified incubation period, the medium was aspirated, and cells were washed three times with PBS (pH 7.4) to remove unbound nanoparticles. Cells were fixed with 3% paraformaldehyde, permeabilised with Triton X-100 (0.01% in PBS) for 5 min and washed with Milli-Q water. Nuclei were stained with DAPI (1 μg mL^{-1}) and FITC (0.001 mol%) was used for nanoparticle labelling. Samples were imaged using confocal microscopy (Carl Zeiss LSM, Germany) at 60× magnification.[38]

2.14. Cell viability assay

The biocompatibility and cytotoxicity of INH, PDX, and the INH–PDX–NEM formulation were evaluated using the 3-(4,5-dimethylthiazol-2-yl)-2,5-diphenyltetrazolium bromide (MTT) assay. To evaluate the cytotoxicity of the antitubercular drugs and their formulations on viable cells, 5×10^5 RPMI-2650 cells were seeded into 96-well microplates (Corning Life Sciences, New York, USA) and cultured for 24 h to allow for cell adherence. After incubation, the cells were washed with PBS and treated with various concentrations (100–500 μg mL^{-1}) of INH, PDX, and INH–PDX–NEM formulation (corresponding to the concentrations of INH and PDX), along with a blank nanoformulation as the control, for 24 h. Then, the medium was aspirated, and 25 μL of MTT solution (1 mg mL^{-1} in PBS) in a serum-free medium was added to each well. The plates were then incubated for 4 h in the dark.

Following incubation, the supernatant was discarded, and 100 μL of DMSO was added to each well to dissolve the formazan crystals. The plates were shaken gently for 10 min at room temperature. The absorbance of formazan crystals was measured at a maximum wavelength of 570 nm using a microplate reader (Synergy H2, BioTek Instruments, USA). Cell viability was assessed as a percentage of untreated control cells.[42]

2.15. Statistical analysis

The experimental data are presented as mean ± standard deviation (SD) based on at least three independent measurements for each trial. Statistical analysis was conducted using one-way ANOVA, with significance thresholds set at $*p < 0.05$, $**p < 0.01$, and $***p < 0.001$. All analyses were performed using the OriginPro 10.1.5.132 (Learning Edition) software (Origin Lab Corp.).

3. Results and discussion

3.1. Preparation and optimisation of the nanoformulation

3.1.1. Preparation of the nanoformulation. The optimised formulation of co-encapsulated INH and PDX in a specified drug ratio was successfully incorporated into a polyelectrolyte complex composed of chitosan and dextran sulfate using a microreactor. The resulting nanoformulation demonstrated in Fig. 1(A) has a mean particle size of 188.18 ± 5.62 nm, a PDI of 0.226 ± 0.01, and a zeta potential (surface charge) of −22.25 ± 3.58 mV. These findings indicate that no significant aggregation occurred in the aqueous medium. Additionally, the surface charge suggests good colloidal stability of the nanosuspension, as shown in Fig. 1(B).

The NPs exhibited high entrapment efficiencies of 82.26 ± 4.36% for INH and 96.28 ± 0.21% for PDX. The loading capacity for INH was 9.28 ± 0.28% w/w, while for PDX, it was 14.86 ± 0.28% w/w, resulting in a total drug loading of 24.14 ± 2.86% w/w, as shown in Table 3. The excellent entrapment efficiency and loading capacity indicate the suitability of the polyelectrolyte complex for nanoparticle fabrication using the microreactor approach.

3.2. Optimisation of the nanoformulation

This study employed a microreactor-assisted approach for the co-encapsulation of INH and PDX, aiming to develop a dry powder formulation to enhance therapeutic outcomes. Several process variables influencing the production of nanoparticles with the desired physical properties were analysed. A Quality by Design (QbD) framework was utilised, incorporating a BBD under the response surface methodology. This approach enabled the efficient evaluation of factors such as chitosan concentration, dextran sulfate, and percentage of PVP-K30 at different levels using a reduced number of experimental trials. Key nanoparticle attributes, such as average particle size, PDI,

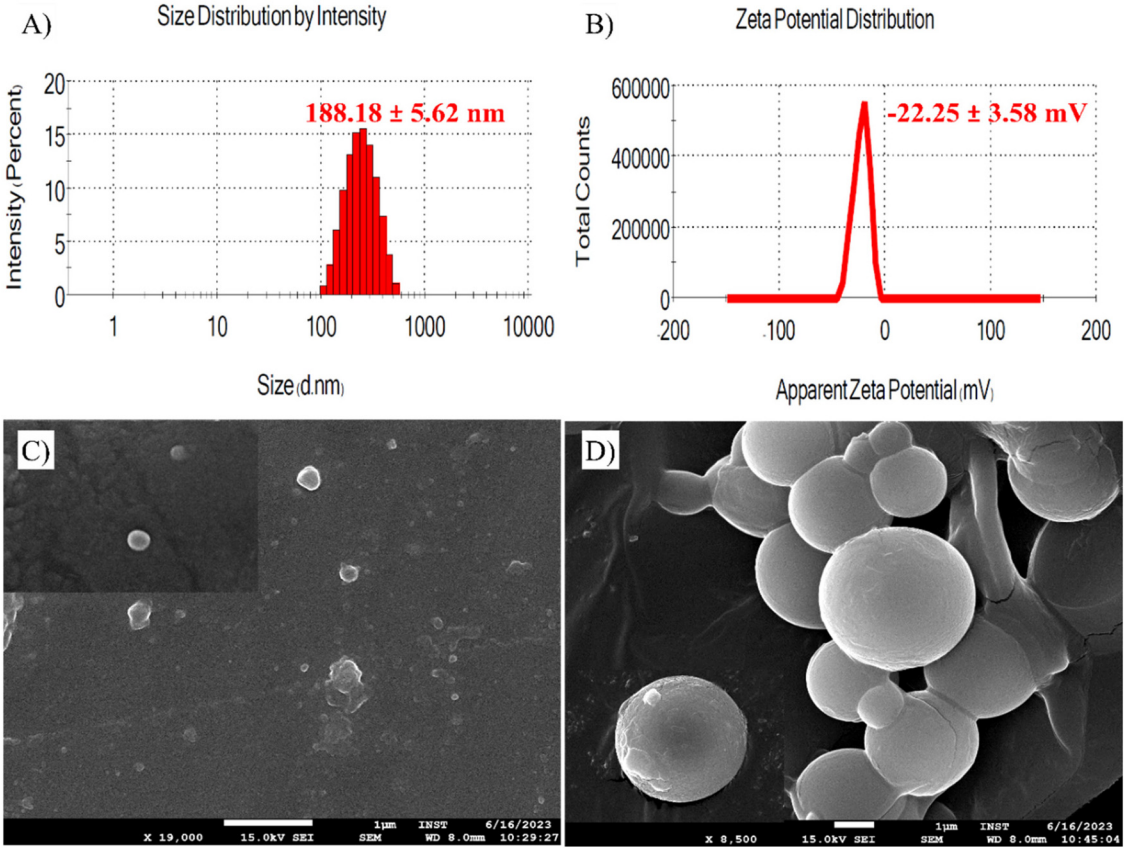

Fig. 1 The physiochemical characterisation of the INH–PDX–COSDSNP formulation: (A) particle size distribution and (B) zeta potential of INH–PDX–COSDSNPs, as determined by dynamic light scattering (DLS); data are represented as mean ± SD (n = 3). (C) SEM images of INH–PDX–COSDSNPs and (D) SEM images of the INH–PDX–NEM spray-dried powder depicting spherical and smooth particles.

Table 3 Physicochemical characteristics of blank COSDS-NPs, INH–PDX–COSDSNPs and INH–PDX–NEM

				Entrapment efficiency (% w/w)		Loading capacity (% w/w)	
Formulations	Particle size	PDI	Zeta potential (mV)	INH	PDX	INH	PDX
Blank COSDS-NPs	176.7 ± 1.6 nm	0.189 ± 0.01	−18.5 ± 0.68	—	—	—	—
INH–PDX–COSDSNPs	188.18 ± 5.6 nm	0.226 ± 0.01	−22.25 ± 3.5	82.26 ± 4.36	96.28 ± 0.21	14.86 ± 0.28	9.28 ± 0.46
INH–PDX–NEM	2.56 ± 0.74 μm	0.202 ± 0.02	−20.25 ± 1.25	86.15 ± 0.54	86.87 ± 0.39	12.24 ± 0.37	9.73 ± 0.4

and zeta potential, were analysed as they are critical to drug release profiles and entrapment efficiency. The formulation process aimed to maximise drug loading while minimising losses. This method facilitated systematic data collection and statistical evaluation, aligning with the goal of creating an optimised drug delivery system for pulmonary administration.[43]

3.3. Statistical optimisation of the DoE

This study explored the outcome of independent variables on the co-encapsulated formulation using a DoE approach, specifically BBD. The results presented in Table 2 were used as cut-off values to evaluate the effect of the independent variables on the dependent variables. Seventeen formulation runs of the co-encapsulated formulation incorporating chitosan and dextran sulfate were carried out and evaluated for key responses, including the mean particle size (Y_1), PDI (Y_2), and zeta potential (Y_3). Data analysis was conducted using Design-Expert® software (version 13.0; State-Ease Inc., Minneapolis, MN, USA). Each response was modelled using a quadratic regression model, and model relevance was evaluated using the multiple correlation coefficient (R^2), analysis of variance (ANOVA), and a lack-of-fit test. The lack-of-fit test was applied to assess data variation around the fitted model, where a p-value greater than 0.05 indicates insignificance relative to pure error. The R^2 value, which reflects the proportion of variation the model explains, should approach 1 to indicate a robust model fit.[44]

3.3.1. Impact on response Y_1. The mean particle size, as shown in Table 2, ranges from 175.9 ± 1.74 nm to 464.16 ±

9.26 nm across different formulations. These data were subjected to ANOVA to determine the most suitable model for predicting the particle size. Table 4 summarises the key features of the fitted linear model, with ANOVA revealing that factors *A* and *B* and their interaction with *C* significantly influenced the nanoparticle size ($p < 0.0014$). The relationship between the particle size (Y_1) and the significant variables is expressed by eqn (4):

$$\text{Particle size} = 234.778 + 16.7825 \times A + -8.11 \times B + 43.8225 \times C \quad (4)$$

A, *B*, and *C* represent COS, DS, and PVP K-30 concentrations, respectively. Factors *A* and *B* negatively impact the particle size, while *C* exhibits a positive effect. Factor *C* had the largest coefficient, indicating a more substantial impact on the nanoparticle size. The mean particle size of the optimised formulation (run 15) was 188.18 ± 5.62 nm. The fabrication method involving a microreactor led to a minimal particle size for this optimised formulation. Fig. 2(A) provides 3D response surface plots, and Fig. 2(B) shows 2D contour plots, illustrating the changes in the particle size in response to varying polymer concentrations (*A* and *B*) and stabiliser percentages.

Table 4 Model statistical fit summary Y_1, Y_2 and Y_3 responses to COSDSNPs developed by BBD

Responses	Source	Sequential *p*-value	Lack of fit *p*-value	Adjusted R^2	Predicted R^2	
Particle size	**Linear**	**0.0014**	**0.0587**	**0.6132**	**0.4181**	**Suggested**
	2FI	0.5084	0.0466	0.5972	0.0220	
	Quadratic	0.3548	0.0377	0.6279	−1.2632	
	Cubic	0.0377		0.9053		**Aliased**
PDI	**Linear**	**0.0486**	**0.2173**	**0.3146**	**−0.0006**	**Suggested**
	2FI	0.6735	0.1604	0.2307	−0.7842	
	Quadratic	0.3495	0.1413	0.2929	−2.6556	
	Cubic	0.1413		0.6414		**Aliased**
Zeta potential	Linear	0.1747	0.0142	0.1484	−0.4056	
	2FI	**0.0133**	**0.0511**	**0.6036**	**−0.0953**	**Suggested**
	Quadratic	0.8204	0.0225	0.4994	−2.1512	
	Cubic	0.0225		0.9021		**Aliased**

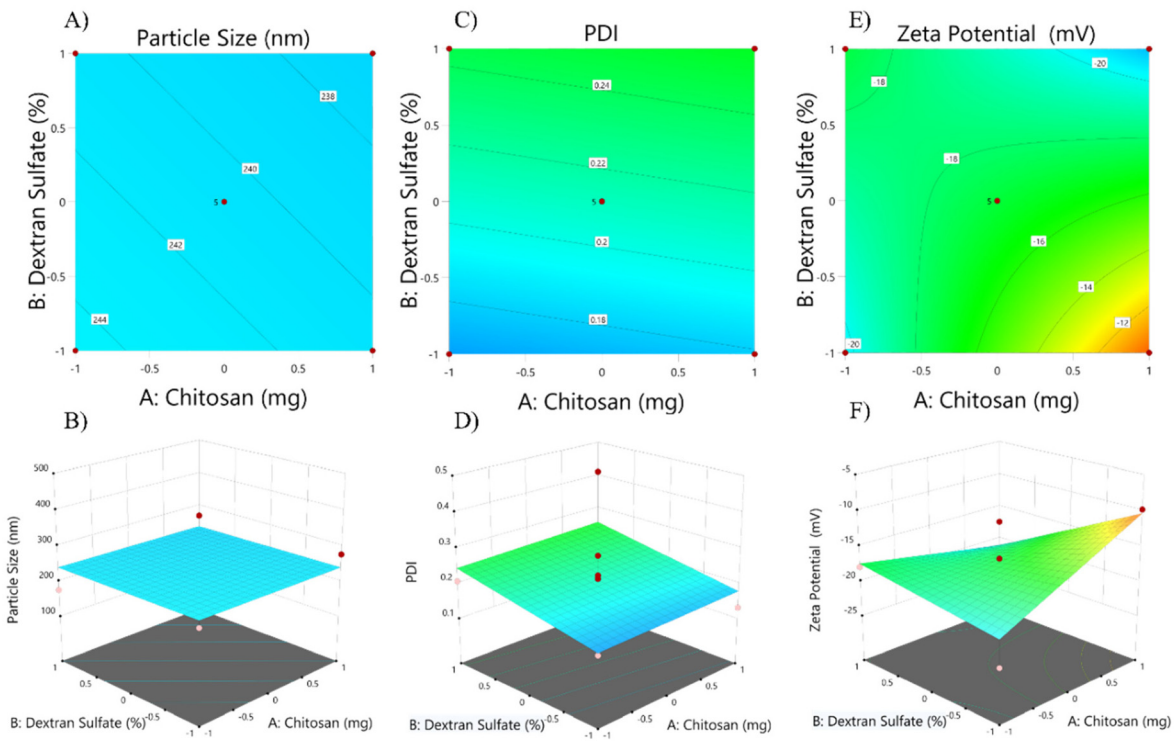

Fig. 2 DoE-based optimisation of INH–PDX–COSDSNPs using the Box–Behnken design featuring 2D contour and 3D response surface plot graphs. The graphs illustrate the influence of the variables on response Y_1 (particle size) (A) and (B), response Y_2 (PDI) (C) and (D), and response Y_3 (zeta potential) (E) and (F).

These visualisations are essential for understanding the interactions between independent variables. Plots were created for all responses to evaluate the effects of the independent variables on the dependent variables. Table 5 presents the ANOVA results for model Y_1, showing a significant interaction between polymer concentrations (A and B) and stabiliser percentage (X_1) on the particle size ($p < 0.0014$). The F-value of the 5.46 model confirms its statistical significance. While the proposed linear model was significant ($p < 0.05$), the lack of fit was not ($p > 0.0587$), suggesting model adequacy for predicting particle size.

3.3.2. Impact on response Y_2. As shown in Table 2, the polydispersity index (PDI) across different formulations ranged from 0.120 ± 0.0008 to 0.412 ± 0.02. Analysis of variance (ANOVA) was used to analyse the data and determine the most appropriate model for predicting the PDI. The characteristics of the fitted linear model are listed in Table 4. The ANOVA results indicated that factors A and B and their interaction with C significantly affected the PDI of nanoparticles ($p < 0.0486$). The relationship between significant variables and PDI (Y_2) is given by the following equation:

$$\text{PDI} = 0.203412 + -0.011375A + 0.0215B + -0.039125C \quad (5)$$

where A, B, and C correspond to the COS, DS, and PVP K-30, respectively. As described in eqn (5), factors A and B positively influence PDI, whereas factor C has a negative effect on PDI. The most significant coefficient for Factor A suggested a strong influence on PDI. The optimised formulation (run 15) had a polydispersity index (PDI) of 0.226 ± 0.01. Using a microreactor in the fabrication method resulted in a minimal PDI for the optimised formulation. Fig. 2(C) presents 3D response surface plots, and Fig. 2(D) shows 2D contour plots, showing how PDI changes with variations in polymer concentrations (A and B) and stabiliser percentage. These plots are essential for understanding the interactions between the independent variables. Response surfaces and contour plots were generated for all responses to evaluate the effects of the independent variables on PDI. The ANOVA results for model Y_2, displayed in Table 5, show that the interaction between polymer concentrations (A and B) and stabiliser percentage (C) significantly influenced PDI ($p < 0.0486$). The F-value of 2.32 supports the statistical significance of the model terms. While the proposed linear model was significant ($p < 0.0486$), the lack of fit was not ($p > 0.2173$), signifying that the model was appropriate for envisaging PDI.

3.3.3. Impact on response Y_3. Based on the experimental data in Table 2, the zeta potential across different formulations varies between −9.8 ± 0.398 mV and 24 ± 0.31 mV. ANOVA was applied to the data to determine the best-fitting model for predicting the zeta potential. The characteristics of the two-factor interaction (2FI) model are presented in Table 4. Analysis of variance indicated that factors A, B, and C and their interactions significantly affected the zeta potential of nanoparticles ($p < 0.0133$). Eqn (6) expresses the relationship between the zeta potential (Y_3) and the significant variables.

$$\begin{aligned}\text{Zeta potential} = &-17.3412 + 1.8375 \times A + -1.45 \times B \\ &+ 1.0125 \times C + -3.175 \times AB \\ &+ 2.7 \times AC + 1.175 \times BC\end{aligned} \quad (6)$$

In this equation, A, B, and C represent COS, DS, and PVP K-30 concentrations, respectively. From the equation, it is observed that A and B have a negative impact on the zeta potential, whereas C has a positive impact. The interaction terms AB and BC had a negative effect, whereas AC positively influenced the zeta potential. The highest coefficient associated with A indicates that this factor has the most significant impact on the zeta potential. The optimised formulation (run 15) had a zeta potential of −22.25 ± 3.58 mV. A polyelectrolyte complex and microreactor fabrication method resulted in a minimised PDI for the optimised formulation. Fig. 2(E) shows a 3D response surface, and Fig. 2(F) presents 2D contour plots, illustrating the variations in zeta potential with varying concentrations of polymers A and B and the stabiliser percentage. These plots are essential tools for visualising the effects of the independent variables and their interactions. They were generated for all responses to assess how the independent variables influenced the zeta potential. The ANOVA results for model Y_3, as presented in Table 5, indicate a significant interaction between polymer concentrations (A and B) and stabiliser percentage (C), with a p-value of <0.0124. The validity of the model was supported by an F-value of 6.08, confirming the statistical significance of its terms. Although the model was not statistically significant ($p < 0.0511$), the lack of fit was not significant, confirming that the model is appropriate for estimating the zeta potential.

Table 5 Summary of ANOVA for Y_1, Y_2, and Y_3 response COSDSNPs prepared by BBD

	Source	df	F-value	p-value	
Particle size (Y_1)	**Model**	**3**	9.46	0.0014	**Significant**
	A-Chitosan	1	3.52	0.0831	
	B-Dextran sulfate	1	0.8228	0.3809	
	C-PVP K-30	1	24.02	0.0003	
	Lack of fit	**9**	5.46	0.0587	**Not significant**
PDI (Y_2)	**Model**	**3**	3.45	0.0486	**Significant**
	A-Chitosan	1	0.6307	0.4414	
	B-Dextran sulfate	1	2.25	0.1572	
	C-PVP K-30	1	7.46	0.0171	
	Lack of fit	**9**	2.32	0.2173	**Not significant**
Zeta potential (Y_3)	**Model**	**6**	5.06	0.0124	**Significant**
	A-Chitosan	1	6.46	0.0293	
	B-Dextran sulfate	1	4.02	0.0728	
	C-PVP K-30	1	1.96	0.1918	
	AB	1	9.64	0.0112	
	AC	1	6.97	0.0247	
	BC	1	1.32	0.2774	
	Lack of fit	**6**	6.08	0.0511	**Not significant**

3.4. Characterisation of spray-dried microparticles

3.4.1. Percentage yield. The percentage yield of spray-dried microparticles from the optimised INH–PDX–NEM formulation (run 15) was calculated to be 48.36% w/w.

3.4.2. Entrapment efficiency. The entrapment efficiency of the prepared nanosuspension (INH–PDX–COSDSNPs) and spray-dried powder (INH–PDX–NEM) was determined by comparing the initial amounts of INH and PDX used with the concentration of free INH and PDX in the supernatant. The entrapment efficiency for INH and PDX in the INH–PDX–NEM of the optimised batch (run 15) was estimated to be 86.15% w/v and 74.87% w/v, respectively, as shown in Table 3.

3.4.3. Particle morphology of spray-dried powder. Surface morphology analysis of the optimised NPs conducted using SEM (Fig. 1C) revealed a spherical shape with a smooth surface. The particle size of the optimised batch after spray drying, determined using SEM, was consistent with the hydrodynamic particle size obtained from DLS analysis. FT-IR analysis confirmed the presence of both INH and PDX within the INH–PDX–NEM formulation, indicating successful encapsulation. The fabricated nanosuspension, following spray drying of INH–PDX–NEM (Run 15), exhibited a smooth and spherical morphology with a uniform particle size distribution, as depicted in Fig. 1D. The mean particle size of the spray-dried INH–PDX–NEM powder was assessed using SEM micrographs. The analysis showed an average particle diameter of 2.19 ± 0.83 μm, with the size distribution ranging approximately from 1 to 3 μm. These findings suggest that the developed nanoformulation has the potential for the co-delivery of INH and PDX in pulmonary TB patients.

3.4.4. Redispersibility index. The redispersibility of INH–PDX–NEM spray-dried microparticles was evaluated by dispersing them back into nanoparticles in an aqueous medium. Upon redispersion, the nanoparticles exhibited a mean particle size of 290.4 ± 4.96 nm, a PDI of 0.375 ± 0.02, and a zeta potential of −11.5 ± 2.08 mV. The redispersibility index (RDI), calculated to assess the efficiency of reconstitution, was approximately 1.54.

Although an RDI value close to 1 would indicate minimal changes upon redispersion, the observed RDI value of 1.54 corresponds to a significant increase in the particle size (~54%) compared to the original nanoparticles. Additionally, the zeta potential decreased to nearly half of its original magnitude, suggesting partial destabilization of the nanoparticles upon reconstitution. These findings indicate that, while redispersion was technically possible, the process led to aggregation and altered surface charge, which may affect the colloidal stability and performance of the nanoparticles.

3.5. Solid state characterisation

3.5.1. Fourier transform infrared spectroscopy (ATR-FTIR). FTIR analysis of INH–PDX–NEM revealed significant molecular interactions and cross-linking processes (Fig. 3A). Distinctive peaks were observed in the COS spectrum, including a broad O–H/N–H stretching vibration at 3353 cm^{-1} and N–H stretching at 3267 cm^{-1}, confirming the presence of hydroxyl and amino groups. Characteristic N–H bending of primary amines appeared at 1599 cm^{-1}, while the saccharide structure showed C–O stretching at 1037 cm^{-1}. The polysaccharide backbone was further evidenced by C–O–C stretching vibrations.[45] The DS spec-

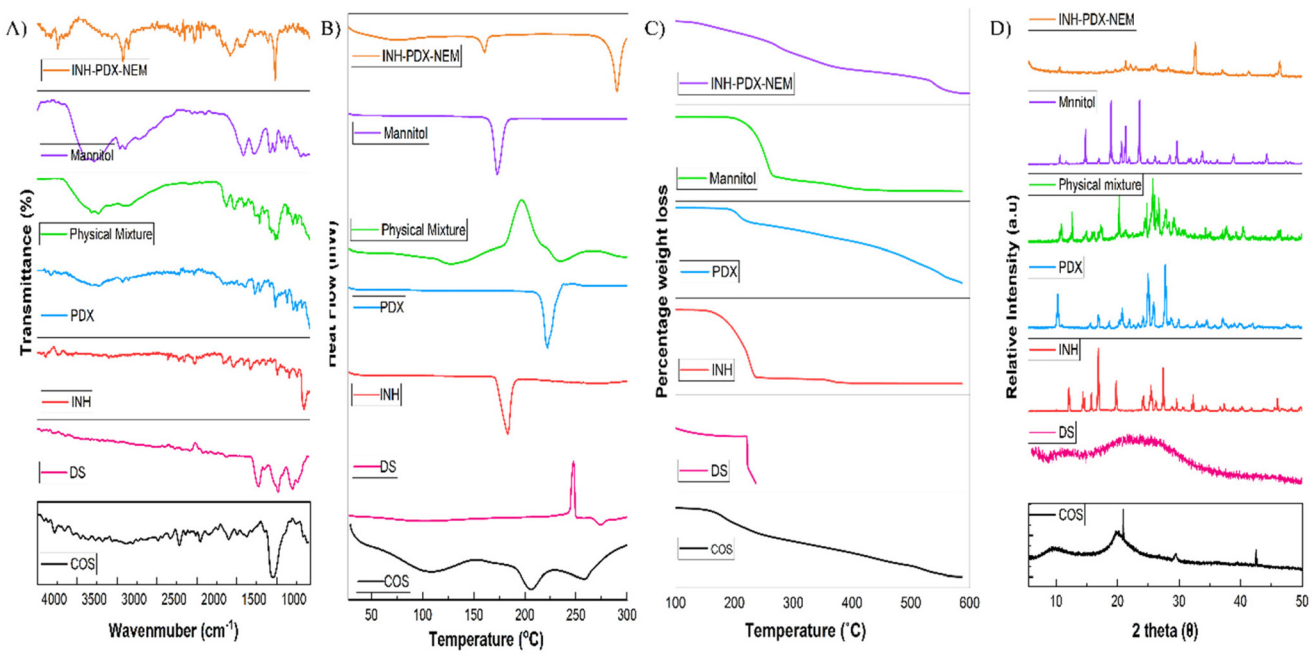

Fig. 3 Formulation and solid-state characterisation of pure INH, PDX, COS, DS, mannitol, and INH–PDX–NEM formulations. (A) FTIR spectra, (B) DSC thermographs, (C) TGA thermographs, and (D) XRD patterns of the INH–PDX–NEM spray-dried powder and excipients.

trum displayed characteristic sulfate group vibrations with asymmetric S=O stretching at 1228 cm^{-1} and symmetric C–O–S stretching at 840 cm^{-1}.[46] The INH spectrum showed N–H stretching at 3325 cm^{-1} and C=O stretching at 1648 cm^{-1}, while PDX exhibited O–H stretching at 3393 cm^{-1} and C=N stretching at 1691 cm^{-1}.[47,48] In the formulated INH–PDX–NEM, several key spectral changes were observed. The N–H stretching of INH shifted to 3365 cm^{-1}, suggesting hydrogen-bonding interactions. The asymmetric S=O stretching of DS shifted from 1228 cm^{-1} to 1254 cm^{-1}, indicating electrostatic interactions between the sulfate groups of DS and amine groups of COS. Importantly, all original component peaks remained detectable in the formulation spectrum, confirming the preservation of the chemical structure.[49] The stability of INH–PDX–NEM appears to result primarily from these ionic and intermolecular interactions rather than chemical cross-linking.

3.5.2. Differential scanning calorimetry (DSC). A DSC thermogram was used to assess the crystallinity of the substances. The INH, PDX, COS, DS, and mannitol thermograms closely aligned with previously reported data, as depicted in Fig. 3(B). In the DSC thermograms of INH and PDX, distinct sharp endothermic peaks were observed at 181.2 °C and 222.2 °C, corresponding to their respective melting points. The thermogram of chitosan oligosaccharide exhibited a broad endothermic peak at 109.1 °C, likely due to moisture evaporation, followed by another endothermic peak at 205.9 °C, attributed to polymer decomposition.[50] The thermogram of dextran sulphate displayed an exothermic peak at 247.9 °C, followed by an endothermic peak at 274.4 °C, indicative of the semicrystalline nature of the dextran sulphate powder used in this DSC analysis.[51]

In contrast, the mannitol endothermic peak at 173.1 °C was observed, corresponding to its melting point.[52] A small endothermic peak at 160.8 °C, observed in the thermogram of the optimised INH–PDX–NEM formulation (run 15), was consistent with the endothermic peak of mannitol. After spray drying, the endothermic peak of mannitol shifted, likely due to melting point depression caused by the reduced particle size of mannitol.[53] Additionally, another endothermic peak appeared at 290.2 °C and shifted to a higher temperature range, suggesting the encapsulation of drugs within the polyelectrolyte complex, resulting in particles in an amorphous state. The absence of endothermic peaks corresponding to the drugs indicates a reduction in the crystallinity of the optimised formulation.

3.5.3. Thermogravimetric analysis (TGA). The thermal stability of the fabricated nanoformulations was assessed using TGA. Fig. 3(C) presents the TGA data for various formulation components, including INH, PDX, COS, DS, mannitol, and the optimised INH–PDX–NEM formulation (run 15). In the first phase, weight loss was observed in the temperature range of 30–200 °C for the drugs, excipients, and formulation, which was likely due to moisture evaporation. In the second phase, a rapid weight loss occurred between 200 and 350 °C, which may be attributed to the release of small molecules such as NH_3. In the third and final phases, complete weight loss was observed for pure drugs and excipients. However, the optimised formulation showed a slight reduction in weight loss within the 350–700 °C range, possibly due to the degradation of the polyelectrolyte complex formed by the INH–PDX–NEM nanoformulation.[46] Furthermore, a significant difference in thermal behaviour was noted between the pure drugs, excipients, and the optimised formulation (run 15) in the final stage of heating. This difference is likely due to the formation of a polyelectrolyte complex between COS and DS, which encapsulates INH and PDX. While nearly 99.90% of the pure components were exhausted by the end of the process, the optimised formulation retained 29.28% residue, suggesting incomplete degradation of the polyelectrolyte complex. In the latter phase of the reaction (350–700 °C), the degradation patterns of the pure drugs, excipients, and optimised formulations were similar. These findings suggest that the drug molecules were effectively incorporated into the polyelectrolyte complex of the INH–PDX–NEM formulation, and the drug molecules were probably exposed after degradation of the outer layer of the polymer matrix. This trend towards greater residual mass suggests that the optimised formulation has improved the thermal stability of the encapsulated drugs within the polyelectrolyte complex, likely due to the conjugation or cross-linking between COS and DS.

3.5.4. X-ray diffraction analysis. The X-ray diffraction (XRD) patterns of COS, DS, INH, PDX, mannitol, and the INH–PDX–NEM formulation are shown in Fig. 3(D). The diffractogram of the nanoformulation exhibited peaks at 10.66°, 18.2°, 19.68°, 20.74°, 21.32°, 22.18°, 23.03°, 25.62°, 26.18°, 28.26°, 32.62°, 37.02°, 41.32°, 46.36°, and 57.42° (2θ), along with a broad halo between 20 and 30° (2θ). Mannitol displayed characteristic crystalline peaks at 10.66°, 14.81°, 18.95°, 20.65°, 21.27°, 23.57°, 26.12°, 28.47°, 29.63°, 31.94°, 33.87°, 38.86°, and 44.22° (2θ). The sharp peaks observed in the diffraction pattern of the formulation confirmed the crystalline structure of both the formulation and mannitol.

Pure INH showed crystalline peaks at 12.06°, 14.36°, 14.63°, 16.88°, 19.77°, 24.20°, 25.60°, 27.63°, 29.57°, 32.24°, 33.87°, 34.41°, 41.80°, and 45.98° (2θ), while PDX exhibited peaks at 10.29°, 16.87°, 20.78°, 15.7°, 24.15°, 24.95°, 25.91°, 27.74°, 37.11°, and 53.44° (2θ). Both COS and DS showed completely amorphous patterns.[54] In the INH–PDX–NEM formulation, several peaks corresponding to INH, PDX, and mannitol were retained (*e.g.*, 19.68°, 20.74°, 21.32°, 23.03°, 25.62°, and 28.26°), although their intensities were reduced compared to the pure components. The presence of a broad halo in the 20–30° (2θ) region suggests partial amorphisation and reduced overall crystallinity. These findings indicate that the spray-drying process altered the solid-state properties of the formulation components.

3.6. *In vitro* aerosolization performance

The *in vitro* deposition profile of the INH–PDX–NEM powder, prepared *via* spray drying, was analysed across various stages of NGI. The corresponding aerosolization parameters are listed in Table 7. Aerodynamic characteristics, including the emitted dose (ED), mass median aerodynamic diameter (MMAD), geo-

metric standard deviation (GSD), and fine particle fraction (FPF), were evaluated. Incorporating a preseparator in the APSD measurements prevented large carrier particles from reaching the upper stages of the impactor, thereby improving the precision of fine particle fraction determination for the spray-dried powders. These findings indicate that INH–PDX–NEM exhibits optimal aerosol properties, making it suitable for pulmonary drug delivery.

The deposition profile showed a significant fraction of particles below the NGI cut-off of 4.46 μm, allowing efficient dispersion throughout the lung regions. Fig. 4A illustrates the deposition of INH–PDX–NEM particles at each NGI stage, with particles in the 1–5 μm range effectively targeting the alveolar region.

Table 7 Aerodynamic characteristics

Aerodynamic properties	Formulation
MMAD (μm)	5.97 ± 1.10
GSD	1.73 ± 0.23
FPF (%)	36.63 ± 3.12

Optimisation of these aerodynamic parameters in the spray-dried INH–PDX–NEM formulation (Run 15) yielded a high emitted dose (>90%), enabling effective passive inhalation in the experimental models. The MMAD for the optimised batch was measured at 5.97 ± 1.10 μm, facilitating deposition in the alveolar region. Additionally, the FPF was 36.63 ± 3.12%, meaning that approximately 36% of the particles fell into the fine particle category, which is essential for lower respiratory deposition where Mtb resides.

A GSD of 1.73 ± 0.23 indicates a relatively narrow aerodynamic size distribution and enhanced consistency in lung deposition (Table 7). Comparative studies have demonstrated the potential of INH–PDX–NEM powder for inhalation therapy. For instance, Jadhav *et al.* reported that clofazimine nanocrystals showed suitable aerodynamic properties (MMAD of 5.80 ± 0.57 μm, FPF > 43.9 ± 2.46%, and ED ≥ 80%) for TB treatment.[55] Patil *et al.* highlighted the potential of a spray-dried nanoformulation for inhalation containing bedaquiline and pyrazinamide, which displayed optimal aerodynamic characteristics. The MMAD for bedaquiline and pyrazinamide were recorded at 2.16 ± 0.39 μm and 2.39 ± 0.06 μm, respectively, with a FPF greater than 75%, demonstrating excellent aerosolization suitability for targeted TB therapy.[5]

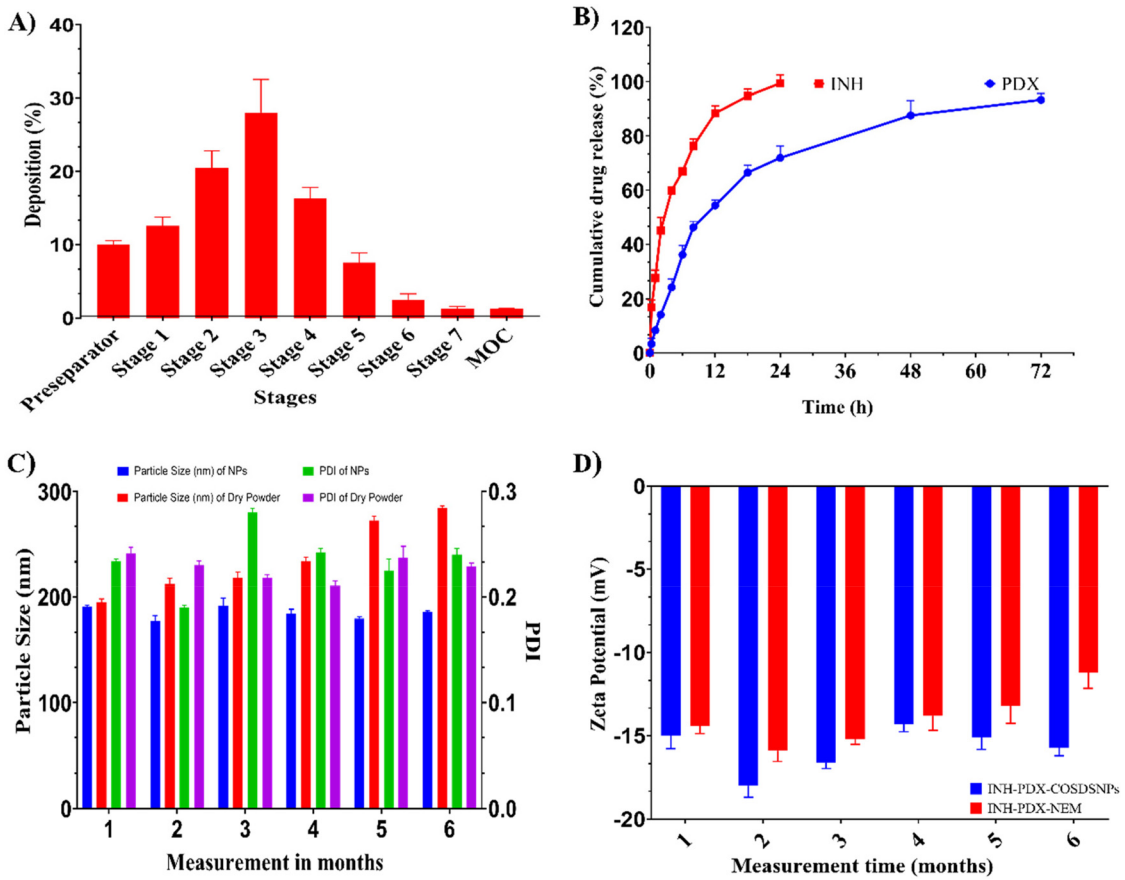

Fig. 4 (A) *In vitro* pulmonary lung deposition pattern of the INH–PDX–NEM dry powder as the percent emitted dose (ED) in each stage of NGI data. Data are presented as mean ± SD (n = 3). (B) *In vitro* drug release profiles of INH and PDX from INH–PDX–NEM. (C and D) Stability study of INH–PDX–COSDSNPs and INH–PDX–NEM dry powder as mean particle size, mean PDI, and mean zeta potential. The data are presented as mean ± SD (n = 3).

The spray-dried INH–PDX–NEM powder enables targeted lung delivery as an inhalable dry powder, with optimised particles (MMAD < 5 μm, high FPF) for deep alveolar deposition, which is crucial for effective TB treatment.

3.7. *In vitro* drug release study

The drug release study was conducted in PBS at pH 7.4; the release profile of INH demonstrated a slightly faster initial rate than PDX.[56] Pure INH and PDX were fully released within 2 h and 1.5 h, respectively. In contrast, the INH–PDX–NEM formulation exhibited prolonged release, which was sustained for up to 24 h and 72 h, respectively.

During the first 4 h, the spray-dried powder formulation exhibited an initial burst release of approximately 27% and 24% for INH and PDX, respectively. The rapid initial release of INH and PDX could be attributed to the migration of drug molecules from the particle core to the shell.[57] Although isoniazid (INH) is hydrophilic, the hydrazide moiety enables it to establish hydrogen bonding with the polymer matrix, which enhances its retention during nanoparticle fabrication. In contrast, pyridoxine hydrochloride (PDX), being a highly water-soluble protonated salt, has minimal affinity for the hydrophobic regions of the carrier, leading to greater migration into the external aqueous phase and consequently lower entrapment efficiency—a pattern frequently noted for hydrophilic drugs prepared by double-emulsion or solvent-evaporation techniques.[58–60] These differences in EE are reflected in the release profiles (Fig. 4B): INH exhibited 98.71% release within 24 h, whereas PDX showed 93.33% release at 72 h. The relatively higher EE of INH likely contributed to its more rapid cumulative release, while the lower EE of PDX reduced its initial burst and prolonged its release, indicating a sustained-release pattern for both drugs. This may result from the dissolution rates of the drugs being modulated by the protective shell formed by the polyelectrolyte complex, which decreases the release rates of both drugs.[61]

3.8. *In vitro* drug release kinetics

The drug release kinetics of nano-embedded microparticles fabricated from the polyelectrolyte complex of COS and DS revealed discrete release mechanisms for INH–PDX–NEM encapsulated in the polymeric matrix. Various mathematical kinetic models, such as zero-order, first-order, Higuchi, Hixon–Crowell, and Korsmeyer–Peppas, were applied to the release data to evaluate the best-fit model and to understand the release mechanisms of both drugs, as shown in Table 6.

Table 6 Release kinetic models of INH and PDX loaded spray-dried powder

Dry powder inhalation	Zero order R^2	First order R^2	Higuchi model R^2	Hixon–Crowell model R^2	Korsmeyer–Peppas model R^2
Release of INH	0.8795	0.9705	0.9896	0.9468	0.7853
Release of PDX	0.9968	0.9963	0.9507	0.9375	0.8268

For INH, the release kinetics of INH formed the COS–DS polymeric complex, and the Higuchi model with the highest R^2 value of 0.9896 was observed as the best fit, indicating a diffusion-dominated release mechanism and characteristics of the matrix system in which INH diffuses through the porous structure. Additionally, the first-order model (R^2 value: 0.9705) denotes the secondary contribution from the concentration-dependent release mechanism, while the Hixson–Crowell model (R^2 value: 0.9468) highlights the release mechanism driven by surface erosion as the polymeric complex dissolves and reduces in size. Furthermore, the zero-order model also showed a relatively high fit (R^2 value: 0.8795), implying some degree of constant release of INH, but this is not the dominant release mechanism. However, the Korsmeyer–Peppas model (R^2 value: 0.8268) offers limited pertinency. The release kinetic study of INH shows multifaceted behaviour, typical of polyelectrolyte complexes.

In contrast, for PDX, the zero-order model had a high R^2 value of 0.9968, suggesting a constant release rate, potentially due to matrix erosion or swelling. The first-order (R^2; 0.9963) and Hixson–Crowell models (R^2; 0.9375) for PDX indicated some degree of concentration-dependent or diffusion-based release mechanisms. Moreover, the Korsmeyer–Peppas model with an R^2 value of 0.8268 and the Higuchi model with an R^2 value of 0.9507 indicated that these models did not align well with the observed PDX release profile.[43]

These findings suggest that the Hixson–Crowell model best explains INH release *via* surface erosion, whereas the zero-order model captures the steady release rate of PDX, which is likely due to matrix erosion. The release kinetic analysis highlights the expediency of a multi-model approach to depict the drug release dynamics from INH–PDX–NEM, with each model providing insights into how co-delivered drugs interact with the polymeric matrix.[62]

3.9. Stability studies

Stability studies were conducted on the optimised INH–PDX–COSDSNPs (nanosuspension) and INH–PDX–NEM (microparticles as dry powder) over a period of six months at room temperature (25 ± 2 °C). The particle size, polydispersity index (PDI), and zeta potential were assessed at 0, 1, 2, 3, 4, 5, and 6 months. These parameters did not change significantly during the study period, indicating sustained stability. These parameters, particularly the particle size, PDI, and zeta potential, were selected as indicators of hydrostability. Numerical values were recorded to assess alterations, with no observable changes in the colour of the nanosuspension-containing nanoparticles. Fig. 4(C) and (D) illustrate the data for the mean particle size, PDI, and zeta potential. The nanosuspension stabilized with PVP-K30 exhibited an average particle size of 185.84 ± 5 nm and a low PDI of 0.227 ± 0.020, indicating particle homogeneity. The stability results for the INH–PDX–NEM dry powder formulation showed an increase in particle size from 284 to 378 nm, an increase in PDI from 0.230 to 0.324, and a zeta potential measurement of −18.26 mV, indicating that the formulation remained stable. In addition, the

negative zeta potential suggests an acceptable colloidal stability. Notably, both the INH–PDX–COSDSNPs and INH–PDX–NEM formulations demonstrated superior stability over 6 months, regardless of room temperature conditions.[63] These findings support the stability of the formulation at room temperature, eliminating the need for cold storage, which is particularly beneficial for distribution in regions with high TB prevalence, such as low- and middle-income countries.

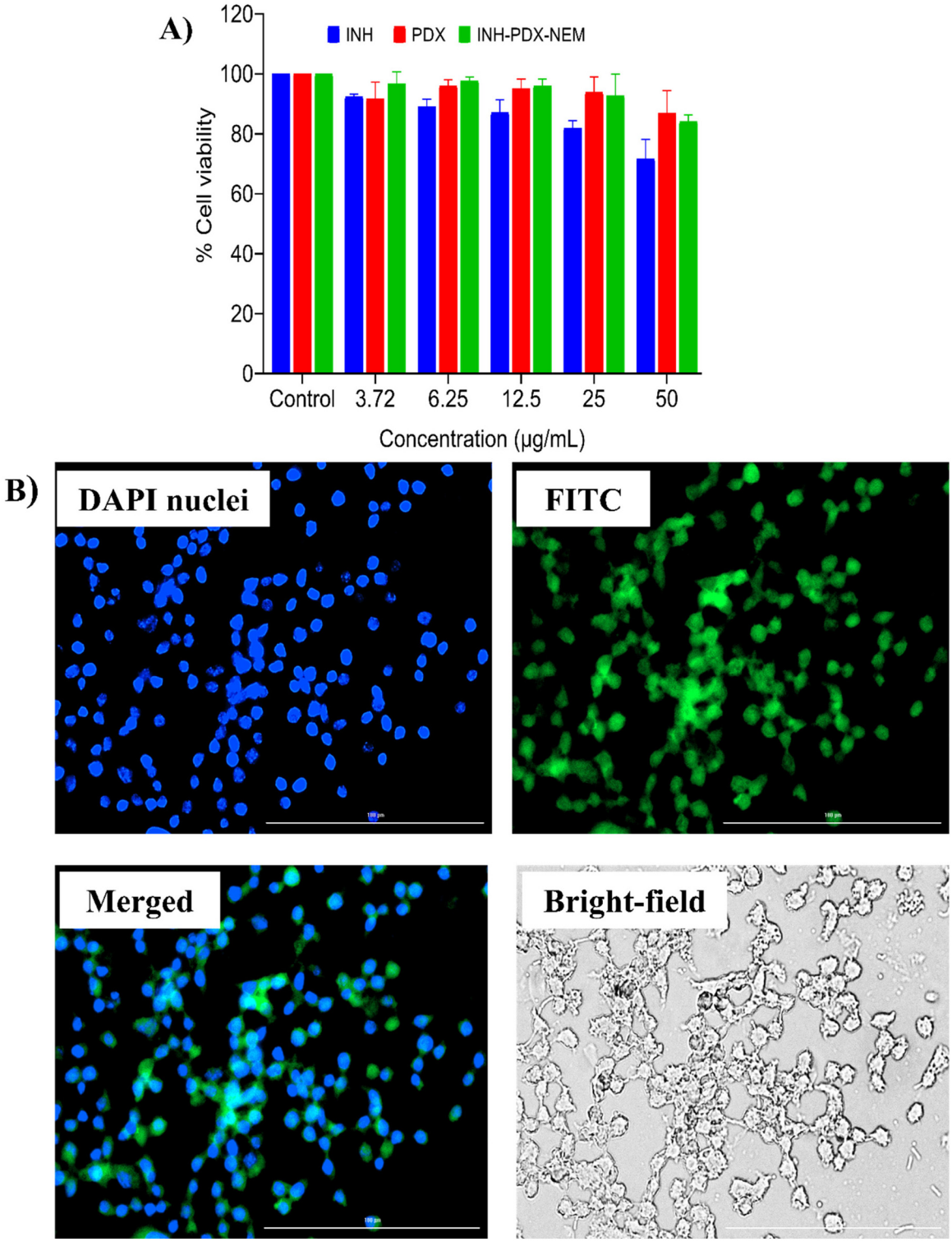

Fig. 5 (A) The cytotoxicity of INH, PDX, and the INH–PDX–NEM formulation was assessed in RAW 264.7 cells using the MTT assay to evaluate cell viability. (B) Cellular uptake studies were performed to investigate the internalization of FITC-labelled nanoparticles in RAW 264.7 macrophages.

3.10. Antitubercular activity

The minimum inhibitory concentration (MIC) and half-maximal inhibitory concentration (IC_{50}) values for INH and its INH–PDX–NEM powder formulation against Mtb strain MTCC 300 provided important insights into their antimicrobial effectiveness. The MIC for INH was 5 μg mL^{-1}, indicating that this concentration was sufficient to inhibit the growth of Mtb. However, the IC_{50} value of 394.1 μg mL^{-1} suggests that a significantly higher concentration is required to achieve a 50% reduction in cell viability, highlighting that while INH is effective at low concentrations for bacterial growth inhibition, higher doses may be required for optimal therapeutic outcomes. In contrast, the INH–PDX–NEM powder formulation demonstrates a considerably lower MIC of approximately 0.5 μg mL^{-1}, indicating enhanced efficacy against Mtb compared to pure INH. Furthermore, the IC_{50} value of the nanoformulation was 201.6 μg mL^{-1}, suggesting that it can achieve a 50% reduction in cell viability at a lower concentration than that required for pure INH. Moreover, Saifullah *et al.* previously reported the MIC of pure ethambutol and its nanoformulation against *M. smegmatis* using the resazurin microtiter assay. The study revealed an effective MIC of 2.1 μg mL^{-1} for the nanoformulation, indicating its retained antitubercular activity.[64] These results indicate that the nanoformulation not only exhibits superior antibacterial activity but also presents a more favourable safety profile, making it a potentially more effective therapeutic option, particularly for drug-resistant strains of Mtb. Overall, these findings highlight the potential of the nanoformulation to improve the therapeutic efficacy of INH in combating TB.[65]

3.11. Cell viability assay

Cell viability assays using RAW 264.7 macrophages were conducted to evaluate the biocompatibility of pure drugs and their INH–PDX–NEM formulations (Fig. 5A). Both pure INH and PDX and their corresponding nano-embedded formulations exhibited minimal cytotoxicity at the tested concentrations. However, at the highest concentration of 25 μg mL^{-1}, pure INH decreased the cell viability to approximately 87%. Notably, the nano-embedded INH formulation showed comparable cell viability, indicating reduced cytotoxicity. Similarly, the INH–PDX–NEM formulation of INH demonstrated marginally lower cytotoxicity than the pure drug.

3.12. Cellular uptake study

Our study evaluated the cellular uptake of FITC-labelled chitosan oligosaccharide-dextran sulfate nanoparticles (COSDSNPs) in RAW 264.7 macrophages using fluorescence microscopy (Fig. 5B). The nanoparticles were covalently labelled with FITC prior to cell exposure through reaction with free amino groups of chitosan oligosaccharide, followed by thorough purification to ensure specific labelling of the nanoparticles rather than nonspecific interactions with cellular components. This labelling approach allowed clear visualization of nanoparticle uptake, with FITC-labelled COSDSNPs exhibiting bright green fluorescence within cells compared to untreated controls. DAPI staining (blue) confirmed intact nuclear morphology, while merged images revealed that the nanoparticles were primarily localized in the cytoplasmic compartment with minimal perinuclear accumulation. We emphasize that this experiment specifically examined nanoparticle–macrophage interactions to establish fundamental uptake mechanisms, as these COSDSNPs will be subsequently incorporated into microparticles for pulmonary delivery in future formulations. The observed cytoplasmic localization demonstrates the nanoparticles' ability to efficiently cross macrophage membranes, a crucial requirement for effective tuberculosis drug delivery.

In another study, Ravindran *et al.* evaluated the cytotoxicity of curdlan sulfate-chitosan nanoparticles (CSC NPs) using the MTT assay in RAW 264.7 cells. The results revealed high cell viability exceeding 85% at concentrations of 10, 25, and 100 μg mL^{-1} over 24 and 48 h. Although a slight decrease in cell viability was observed at the highest concentration (100 μg mL^{-1}), these findings suggest that CSC NPs are non-toxic and may be suitable as a drug delivery system for treating DR-TB.[66] Gnanadhas *et al.* demonstrated the effective treatment of Salmonella infection using ciprofloxacin-loaded CH-DS nanocapsules in the RAW 264.7 cell model. The nanocapsules were biocompatible, as evidenced by the lack of cytotoxicity at concentrations of up to 40 mg mL^{-1}, suggesting their potential for safe therapeutic applications.[67]

4. Conclusions

We successfully developed a co-encapsulated formulation of INH–PDX–NEM powder for pulmonary administration *via* dry powder inhalation. Employing a DoE approach, we optimised the formulation and experimental framework using microreactor technology and spray-drying methods.

We achieved optimal encapsulation of INH and PDX with a chitosan and dextran sulfate polyelectrolyte complex of nanoparticles. Furthermore, the optimisation performed by DoE based on BBD enabled the fine-tuning of the critical process parameters to achieve favourable results.

The resulting NEM dry powder exhibited exceptional pulmonary delivery characteristics following comprehensive optimisation, including improved entrapment efficiency, optimal mean particle size, low polydispersity index (PDI), favourable zeta potential, effective aerosolization, and enhanced stability. Our research underscores the potential of the INH–PDX co-delivery system as a significant therapeutic strategy against tuberculosis as a dry powder formulation tailored for pulmonary delivery. In future work, we plan to conduct *in vivo* studies to evaluate both the antimicrobial efficacy and the neuroprotective potential of the INH–PDX formulation in appropriate animal models.

Conflicts of interest

The authors declare that they have no competing financial interests or personal relationships that could have influenced the work presented in this paper.

Data availability

Data will be made available on a valid request.

Acknowledgements

This study was financially supported by the Anusandhan National Research Foundation (ANRF), New Delhi, India, in terms of Empowerment and Equity Opportunities for Excellence in Science (EEQ/2023/000060). One of the authors is grateful to BARTI, Pune, for providing the Dr Babasaheb Ambedkar National Research Fellowship (BANRF). The authors gratefully acknowledge Lupin, Ltd (Cha. Sambhajinagar, India) for providing a gift of isoniazid. We acknowledge the paid research services and collaboration with Aakaar Biotechnologies Pvt. Ltd, Lucknow, India, for conducting the *in vitro* antitubercular and cytotoxicity assays.

References

1 A. Z. Bahlool, B. Cavanagh, A. O. Sullivan, R. MacLoughlin, J. Keane, M. P. O. Sullivan and S. A. Cryan, *Eur. J. Pharm. Sci.*, 2024, **196**, 106734.
2 K. M. S. R. Sefat, M. Kumar, S. Kehl, R. Kulkarni, A. Leekha, M. M. Paniagua, D. F. Ackart, N. Jones, C. Spencer, B. K. Podell, H. Ouellet and N. Varadarajan, *Vaccine*, 2024, **42**, 125909.
3 C. B. E. Chee, R. Reves, Y. Zhang and R. Belknap, *Respirology*, 2018, **23**, 893–900.
4 A. Mobed, V. Alivirdiloo, S. Gholami, A. Moshari, A. Mousavizade, R. Naderian and F. Ghazi, *Curr. Microbiol.*, 2024, **81**, 1–15.
5 S. M. Patil, A. M. Diorio, P. Kommarajula and N. K. Kunda, *Int. J. Pharm.*, 2024, **653**, 123920.
6 B. M. Warpe, in *Tuberculosis of the Central Nervous System*, Springer International Publishing, Cham, 2017, pp. 339–350.
7 G. B. Migliori, M. C. Raviglione, T. Schaberg, P. D. O. Davies, J. P. Zellweger, M. Grzemska, T. Mihaescu, L. Clancy and L. Casali, *Eur. Respir. J.*, 1999, **14**, 978–992.
8 D. E. Snider, *Tubercle*, 1980, **61**, 191–196.
9 J. G. Kariuki, S. M. Kariuki and P. Angel, *J. Tuberc. Res.*, 2023, **11**, 33–48.
10 G. Fekadu, F. Bekele, K. Bekele, T. Girma, G. Mosisa, M. Gebre, T. Alemu, T. Tekle, B. Gamachu and A. Diriba, *Patient Prefer. Adherence*, 2020, **14**, 1259–1265.
11 U. A. Boelsterli and K. K. Lee, *J. Gastroenterol. Hepatol.*, 2014, **29**, 678–687.
12 G. Wyszogrodzka-Gaweł, P. Dorożyński, S. Giovagnoli, W. Strzempek, E. Pesta, W. P. Węglarz, B. Gil, E. Menaszek and P. Kulinowski, *Pharmaceutics*, 2019, **11**, 687.
13 J. Larkins-Ford and B. B. Aldridge, *Expert Opin. Drug Discovery*, 2023, **18**, 83–97.
14 A. Sultana, M. Zare, V. Thomas, T. S. S. Kumar and S. Ramakrishna, *Med. Drug Discovery*, 2022, **15**, 100134.
15 J. K. Patra, G. Das, L. F. Fraceto, E. V. R. Campos, M. del P. Rodriguez-Torres, L. S. Acosta-Torres, L. A. Diaz-Torres, R. Grillo, M. K. Swamy, S. Sharma, S. Habtemariam and H.-S. Shin, *J. Nanobiotechnol.*, 2018, **16**, 71.
16 B. Tousian and A. R. Khosravi, *Results Chem.*, 2023, **6**, 101146.
17 M. Mukhtar, N. Csaba, S. Robla, R. Varela-Calviño, A. Nagy, K. Burian, D. Kókai and R. Ambrus, *Pharmaceutics*, 2022, **14**, 1543.
18 K. C. Petkar, S. Chavhan, N. Kunda, I. Saleem, S. Somavarapu, K. M. G. G. Taylor and K. K. Sawant, *AAPS PharmSciTech*, 2018, **19**, 1758–1772.
19 S. He, J. Gui, K. Xiong, M. Chen, H. Gao and Y. Fu, *J. Nanobiotechnol.*, 2022, **20**, 101.
20 B. Chaurasiya and Y.-Y. Zhao, *Pharmaceutics*, 2020, **13**, 31.
21 L. Ding, A. D. Brunaugh, S. Stegemann, S. V. Jermain, M. J. Herpin, J. Kalafat and H. D. C. Smyth, *Pharmaceutics*, 2021, **13**, 1213.
22 M. Mukhtar, E. Pallagi, I. Csóka, E. Benke, Á. Farkas, M. Zeeshan, K. Burián, D. Kókai and R. Ambrus, *Int. J. Biol. Macromol.*, 2020, **165**, 3007–3019.
23 S. R. Pardeshi, E. B. Kole, H. S. Kapare, S. M. Chandankar, P. J. Shinde, G. S. Boisa, S. S. Salgaonkar, P. S. Giram, M. P. More, P. Kolimi, D. Nyavanandi, S. Dyawanapelly and V. Junnuthula, *Pharmaceutics*, 2022, **14**, 2632.
24 E. Kole, S. Pardeshi, A. S. Mujumdar and J. Naik, *in Particulate Drying*, CRC Press, Boca Raton, 2023, pp. 131–150.
25 E. Kole, K. Jadhav, R. Singh, S. Mandpe, A. Abhang, R. K. Verma and J. Naik, *Curr. Drug Delivery*, 2025, **22**, 249–260.
26 K. Jadhav, E. Kole, R. Singh, S. K. Rout, R. K. Verma, A. Chatterjee, A. Mujumdar and J. Naik, *Drying Technol.*, 2024, **42**, 1415–1441.
27 E. Kole, K. Jadhav, N. Shirsath, P. Dudhe, R. K. Verma, A. Chatterjee and J. Naik, *J. Drug Delivery Sci. Technol.*, 2023, **81**, 104261.
28 E. Kole, K. Jadhav, Z. Khan, R. K. Verma, A. Chatterjee, A. Mujumdar and J. Naik, *Future J. Pharm. Sci.*, 2024, **10**, 156.
29 P. Guo, B. A. Buttaro, H. Y. Xue, N. T. Tran and H. L. Wong, *Eur. J. Pharm. Biopharm.*, 2020, **151**, 189–198.
30 A. A. Abdelbary and M. H. H. AbouGhaly, *Int. J. Pharm.*, 2015, **485**, 235–243.
31 R. Deshmukh, P. Wagh and J. Naik, *Drying Technol.*, 2016, **34**, 1758–1772.
32 S. Pardeshi, P. Patil, R. Rajput, A. Mujumdar and J. Naik, *Drying Technol.*, 2021, **39**, 337–347.
33 S. Mandpe, E. Kole, V. Parate, A. Chatterjee, A. Mujumdar and J. Naik, *J. Microencapsulation*, 2024, 1–13.
34 G. Khairnar, V. Mokale, R. Khairnar, A. Mujumdar and J. Naik, *Drying Technol.*, 2022, **40**, 626–637.
35 A. Patil, S. Pardeshi, M. Kapase, P. Patil, M. More, S. Dhole, E. Kole, P. Deshmukh, A. Gholap, A. Mujumdar and J. Naik, *Drying Technol.*, 2024, **42**, 661–673.

36 I. Chandrasiri, M. L. Yaddehige, B. Li, Y. Sun, W. E. Meador, A. Dorris, M. F. Zia, N. I. Hammer, A. Flynt, J. H. Delcamp, E. Davis, A. Lippert and D. L. Watkins, *ACS Appl. Polym. Mater.*, 2022, **4**, 2972–2986.
37 S. Mandpe, E. Kole, V. Parate, A. Chatterjee, A. Mujumdar and J. Naik, *Drying Technol.*, 2023, **41**, 2418–2430.
38 K. Jadhav, A. Jhilta, R. Singh, E. Ray, V. Kumar, A. B. Yadav, A. K. Singh and R. K. Verma, *Nanoscale*, 2024, **16**, 16485–16499.
39 Y. Jiang, Y. Zhou, C. Y. Zhang and T. Fang, *Int. J. Nanomed.*, 2020, **15**, 3319–3331.
40 P. Wagh, A. Mujumdar and J. B. Naik, *Part. Sci. Technol.*, 2019, **37**, 347–357.
41 I. R. Scolari, P. L. Páez, M. M. Musri, J. P. Petiti, A. Torres and G. E. Granero, *Drug Delivery Transl. Res.*, 2020, **10**, 1403–1417.
42 A. Sharma, K. Vaghasiya, E. Ray, P. Gupta, A. K. Singh, U. D. Gupta and R. K. Verma, *Int. J. Pharm.*, 2019, **558**, 231–241.
43 D. Verma, P. S. Thakur, S. Padhi, T. Khuroo, S. Talegaonkar and Z. Iqbal, *J. Mol. Liq.*, 2017, **242**, 382–394.
44 P. Yadav, V. Rastogi and A. Verma, *Future J. Pharm. Sci.*, 2020, **6**, 7.
45 T. Gomathi, C. Govindarajan, H. R. M. Rose, P. N. Sudha, P. K. M. Imran, J. Venkatesan and S.-K. Kim, *Int. J. Pharm.*, 2014, **468**, 214–222.
46 C. Chavan, P. Bala, K. Pal and S. N. Kale, *OpenNano*, 2017, **2**, 28–36.
47 N. Changsan and C. Sinsuebpol, *Pharm. Dev. Technol.*, 2021, **26**, 181–192.
48 M. K. Trivedi, A. Branton, D. Trivedi, G. Nayak, R. Singh and S. Jana, *J. Environ. Anal. Toxicol.*, 2015, **5**, 329.
49 V. A. Guarino, A. Blau, J. Alvarenga, J. Loscalzo and Y.-Y. Y. Zhang, *Int. J. Pharm.*, 2021, **610**, 121287.
50 H. M. Anter, I. I. Abu Hashim, W. Awadin and M. M. Meshali, *Int. J. Nanomed.*, 2019, **14**, 4911–4929.
51 B. Sarmento, A. Ribeiro, F. Veiga and D. Ferreira, *Colloids Surf., B*, 2006, **53**, 193–202.
52 S. Manchanda, P. K. Sahoo and D. K. Majumdar, *Nanotechnol. Rev.*, 2016, **5**, 445–453.
53 Z. Shao, K. K. G. Tam, V. P. K. Achalla, E. C. Y. Woon, A. J. Mason, S. F. Chow, W. C. Yam and J. K. W. Lam, *Int. J. Pharm.*, 2024, **654**, 123960.
54 I. Salim, G. M. Khalid, A. S. Wada, S. Danladi, F. S. Kurfi and M. S. Gwarzo, *J. Res. Pharm.*, 2024, **28**(5), 1704–1719.
55 K. Jadhav, A. Jhilta, R. Singh, E. Ray, N. Sharma, R. Shukla, A. K. Singh and R. K. Verma, *Biomater. Adv.*, 2023, **154**, 213594.
56 P. Kaur, V. Mishra, T. Shunmugaperumal, A. K. Goyal, G. Ghosh and G. Rath, *J. Drug Delivery Sci. Technol.*, 2020, **56**, 101502.
57 R. K. Kang, N. Mishr and V. K. Rai, *AAPS PharmSciTech*, 2020, **21**, 48.
58 H. Abd-El-Azim, A. Ramadan, N. Nafee and N. Khalafallah, *J. Liposome Res.*, 2018, **28**, 112–116.
59 B. Rohit and K. I. Pal, *Curr. Nanosci.*, 2013, **9**, 211–220.
60 F. Sciolla, D. Truzzolillo, E. Chauveau, S. Trabalzini, L. Di Marzio, M. Carafa, C. Marianecci, A. Sarra, F. Bordi and S. Sennato, *Colloids Surf., B*, 2021, **208**, 112054.
61 S. W. Ali, F. A. Mangrio, F. Li, P. Dwivedi, M. U. Rajput, R. Ali, M. I. Khan, W. Ding and R. X. Xu, *J. Drug Delivery Sci. Technol.*, 2021, **63**, 102505.
62 T. M. Almeleebia, M. H. Akhter, H. Khalilullah, M. A. Rahman, S. Ahmad, N. Alam, M. S. Ali, G. Khan, I. M. M. Alanazi, N. Shahzad and A. Alalmaie, *ACS Omega*, 2024, **9**, 6845–6860.
63 O. A. Adeleke, R. K. Hayeshi and H. Davids, *Pharmaceutics*, 2020, **12**, 286.
64 B. Saifullah, A. Maitra, A. Chrzastek, B. Naeemullah, S. Fakurazi, S. Bhakta and M. Hussein, *Molecules*, 2017, **22**, 1697.
65 W.-L. Du, S.-S. Niu, Y.-L. Xu, Z.-R. Xu and C.-L. Fan, *Carbohydr. Polym.*, 2009, **75**, 385–389.
66 R. Ravindran, K. Mitra, S. K. Arumugam and M. Doble, *Carbohydr. Polym.*, 2021, **258**, 117686.
67 D. P. Gnanadhas, M. Ben Thomas, M. Elango, A. M. Raichur and D. Chakravortty, *J. Antimicrob. Chemother.*, 2013, **68**, 2576–2586.